Processing of pure copper by powder bed fusion with infrared laser

Results in Engineering 25 (2025) 104497

Contents lists available at ScienceDirect

Results in Engineering

journal homepage: www.sciencedirect.com/journal/results-in-engineering

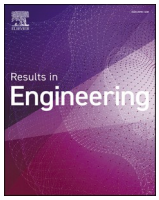

Research paper

Processing of pure copper by powder bed fusion with infrared laser

Flaviana Calignano [a,*], Alessandro Bove [a], Matteo Pavese [b]

[a] Department of Management and Production Engineering (DIGEP), Integrated Additive Manufacturing Center (IAM), Politecnico di Torino, Corso Duca Degli Abruzzi, 24, 10129 Turin, Italy

[b] Department of Applied Science and Technology (DISAT), Politecnico di Torino, Corso Duca Degli Abruzzi, 24, 10129 Turin, Italy

ARTICLE INFO

Keywords:
Copper
Laser power bed fusion
Infrared fiber laser
Deposited energy density

ABSTRACT

The metal laser powder bed fusion (PBF-LB/M) process was used to produce copper (Cu) samples using a conventional single-mode IR fiber laser with a wavelength of 1060–1080 nm and laser power in the range of 185–500 W. As is known in copper laser welding, the creation of surface ripples during keyhole generation affects surface absorption. In this study, the parameters that allow to achieve a keyhole condition to obtain a dense copper sample with an infrared laser were investigated. The deposited energy density allows the parameter window to be identified more precisely with respect to the linear and volumetric energy typically used with the process.

1. Introduction

Among the additive manufacturing (AM) technologies, the laser beam metal powder bed fusion (PBF-LB/M) process has seen widespread use in relevant sectors in recent years, including the medical, automotive, and aerospace industries [1–6], which need a wider range of materials that can meet certain industry needs [7]. A proven advantage of PBF-LB/M over conventional production is the construction of monolithic parts with complex geometries. Geometrical degrees of freedom have the potential to reduce part lead times, costs (no casting, lower energy consumption, material costs), materials and scrap. In the industrial sector, the possibility of using copper with the PBF-LB/M process is arousing more and more interest in the sectors of electronic devices, thermal management systems and aerospace engine structures thanks to the possibility of combining the characteristics of the additive process (greater freedom in design, fine microstructure, etc.) with the excellent electrical properties and thermal conductivity of copper. Most PBF-LB/M machines on the market today use Nd:YAG or fiber lasers with a wavelength between 1064 and 1080 nm. At this wavelength, the pure copper material achieves a reflectivity of over 95 % [8]. The increased reflectivity hinders the metal powder's ability to absorb sufficient laser energy, resulting in inadequate melting and difficulties in powder distribution, leading to increased porosity, spherification, reduced density and poor mechanical and thermal properties of the finished material. In addition, reflected laser light from PBF-LB/M equipment can damage its optical system. Compared to other solid-state lasers, fiber lasers are typically more susceptible to back reflections [9]. Overcoming the high reflectivity is therefore key to melting and forming copper materials with the PBF-LB/M process. The research, also given the requests coming from the various industrial sectors, is trying to find possible solutions and in particular has focused: (i) on the use of lasers with powers of 1 kW [10] and 1.8 kW [11] higher than those currently present on PBF-LB/M systems (200 W and 400 W [12–14]); (ii) act on the process parameters using a specific particle size distribution of the powder [15]; (iii) use a green or blue light laser (wavelength of 515 nm and 450 nm respectively) which absorb approximately 40–45 % of the energy at room temperature [16–19]; (vi) improve the optical absorption of the powder through a layered structure on the powder surface [20]. However, although green lasers improve absorption, the defects created are comparable to those found with infrared lasers at the same laser power. For example, Wang et al. [18] investigated the laser powder bed fusion of pure copper using a green laser with a 532 nm wavelength and a fine spot of 40 μm. The analysis revealed that the sample displayed numerous voids when examined using CT scanning, even though it recorded a density of 96.7 % according to Archimedes' technique and 97.9 % based on CT image data. For laser powers below 450 W and scanning speeds between 300 and 110 mm/s, the components showed defects such as lack of fusion and keyhole. Porosity defects are evenly distributed and large-sides unfused defects have been reduced by increasing laser power (500 W), although there are still many keyhole porosities. Romano et al. [19] uses a powder bed laser melting system equipped with a high-power green

* Corresponding author.
E-mail address: flaviana.calignano@polito.it (F. Calignano).

https://doi.org/10.1016/j.rineng.2025.104497
Received 11 January 2025; Received in revised form 21 February 2025; Accepted 23 February 2025
Available online 24 February 2025

laser source developed to improve the processability of pure copper. The research concentrates on examining membranes that have a specified thickness between 0.5 and 2.5 mm. Despite the density recorded using Archimedes' technique being approximately 99.34 %, the efficacy of these membranes have been compromised by residual porosity resulting from gas entrapment and inadequate melting of the powder throughout the printing phase. Jadhav et al. [21] used an intentionally oxidized copper powder on the surface in a 500 W PBF-LB/M system to improve optical absorption at the infrared fiber laser wavelength. The results showed densities greater than 97.5 % with optical absorption. Jadhav et al. [22] investigated the effect of optically absorptive carburized CuCr1 powder on the copper powder for the fabrication of copper parts. During the PBF-LB/M process, the optimization of the detachment of the modified layer from the surface of the carburized CuCr1 powder and the presence of the chromium and chromium carbide phases inside the cemented layer which can be easily wetted by the liquid copper, allowed the laser beam to interact directly with the modified layer optically absorbent and thermally stable, thus allowing copper parts to be fabricated with a density greater than 98 % using a laser power of less than 300 W.

Some studies on laser welding of copper have shown that the creation of surface ripples during keyhole generation affects surface absorption [23,24]. Furthermore, Jae et al. showed that light absorption is increased by the multi-reflections effect in the keyhole [25]. Engler et al. [26] compared the green laser to the infrared one for welding copper. They found that when a keyhole forms in the weld pool, the lasers, despite welding at two different wavelengths, have similar energy coupling efficiencies, i.e., about 70–80 %.

The basic idea in this study, therefore, is to be able to form the keyhole to reach those energy values that allow the infrared laser wavelength to be used with copper with powers lower than 500 W. This would allow companies already equipped with these systems to be able to produce copper parts, should they need them, without having to make a further investment in machines with more powerful lasers or green and blue lasers that still present the same problems of porosity [18,19].

2. Materials and methods

2.1. Methodology

Each layer previously melted during the PBF-LB/M process creates a surface roughness which improves laser absorption. Another important effect that improves absorption, like in the case of laser welding, is the formation of a keyhole, where multi-reflection can occur. If the melt pool is shallow, instead, the reflection will be directed towards the surrounding environment (conduction-controlled melt pool), and it will not be possible to have an optimal joining between the various layers. Fig. 1 shows a schematic illustration of the relationship between the melt pool aspect ratio and the effective laser absorption. The conduction-controlled melt pool geometry (Fig. 1a) does not allow laser light to penetrate deeply into the melt pool, nor does it allow laser light to reflect internally within the melt pool. So, the effective laser absorption in the conduction regime is mainly governed by the optical absorption of the material, while in the keyhole regime (Fig. 1b) it is mainly governed by the keyhole characteristic followed by the optical absorption of the material. If, however, the melt pool proportions exceed a certain value, the keyhole-induced porosity condition can occur (Fig. 1c). Keyhole stability during the PBF-LB/M process is maintained by achieving a balance between the ablation or recoil pressure that allows the keyhole to open and the keyhole closing forces, i.e., surface tension, convection pressure and hydrostatic pressure [27–30]. The high thermal conductivity of copper allows for the rapid dissipation of absorbed heat, and this can lead, during solidification, to a rapid increase in the closing forces of the keyhole at the top of the melt pool [28]. Furthermore, the increased keyhole closing forces are assisted by the uneven distribution of laser energy along the keyhole wall due to the high reflectivity of copper [31]. Therefore, for highly conductive metals such as copper, during solidification, a relatively shorter time is available for filling, i.e., a molten pool formed from a highly conductive metal will solidify faster than a molten pool consisting of a low conductivity. This results in an increased possibility of trapping vapor bubbles during solidification of the melt which results in keyhole induced porosity formation. This could limit the removal of inclusions through the occurrence of remelting and buoyancy forces during processing of subsequent layers.

In the stable keyhole mode in joining processes, such as welding and PBF-LB/M, the energy coupling of the process is "cavity-enhanced" [33], which makes it possible to weld sheet metals of several millimeters thick or ensure material continuity between successive layers in PBF-LB/M. This highlights a competition between two antagonistic phenomena that can occur in the fusion pool: keyhole penetration and keyhole opening. The recoil pressure promotes keyhole penetration, and the beam trapping effect enhances it. Simultaneously, the keyhole opens as a result of the fusion flow and different driving forces can promote its opening, at the expense of energy coupling (there are less multi-reflection) and potentially, keyhole penetration [34]. During the transition from conduction to keyhole, this competition occurs until an equilibrium is found.

The laser power density, also known as irradiance, I (power per unit area,) and energy density E_d (energy per unit area, also known as

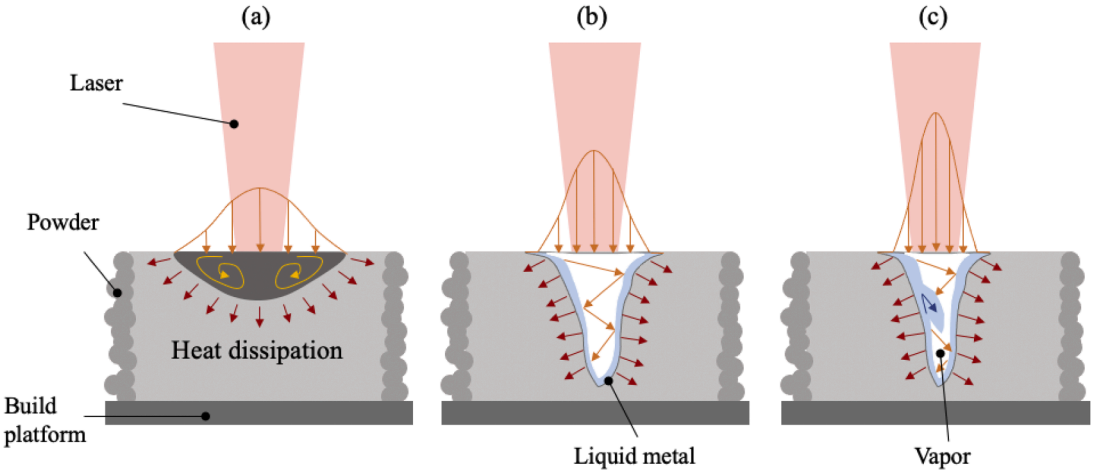

Fig. 1. Schematic illustration of (a) a conduction-controlled, (b) keyhole without porosity, and (c) keyhole-induced porosity melt pools. The schematics presented are adapted from [32].

fluence) are defined by Eq. (1) and 2 [35,36]:

$$I = \frac{P}{area} = \frac{4 \times P}{\pi \times d^2} \left[\mathrm{W} / \mathrm{cm}^2\right] \quad (1)$$

$$E_d = I \times \tau \left[\mathrm{J} / \mathrm{cm}^2\right] \quad (2)$$

Where P, d, and τ are the laser power, laser beam diameter, and laser exposure time respectively. Power density indicates the degree of concentration of the laser output. The energy density, also referred to in the literature as power intensity [37,38], is the energy available for exposure of a melting line by laser. Analyzing the studies in the literature on copper [39–41], it emerged that in order to have a density greater than 98 % a power intensity about 4.5×10^6 W/cm^2 must be used. However, what has emerged from the literature on welding is that the depth of a weld is a function of the enthalpy of the material [42]: the material cannot become a weld or vaporize unless the local enthalpy of the material is large enough to allow phase change. This suggests that it is necessary to consider material and thermodynamic parameters as well as laser properties. Therefore, it was decided to use the normalised enthalpy, which is the ratio of the deposited energy density (ΔH) to the melting enthalpy (h_m), originally proposed by Hann et al. [42] and then modified by Suzuki et al. [43], which is a function of the material, the laser and the thermodynamic parameters :

$$\frac{\Delta H}{h_m} = \frac{AP}{h_m \sqrt{\pi \alpha v r^3}} \text{ where } h_m = \frac{k \cdot \Delta T}{\alpha} \quad (3)$$

Where A is the laser absorptivity, r is the laser beam radius, α is the thermal diffusivity, k is the thermal conductivity, and ΔT is the temperature required to melt the material. Eq. (3) has been used in the literature to define the thresholds keyhole mode melting [27] and related to the front keyhole wall (FKW) angle [44]. According to Huang et al. [44], FKW well defines the keyhole regimes. Furthermore, Gan et al. [45] found that the tangent of FKW angle is approximately proportional to the keyhole number Ke ($Ke = (1/\sqrt{\pi}) \cdot \Delta H / h_m$), which is a scaled version of the normalised enthalpy.

ΔH has the same unit (Joule per unit volume) as the volumetric energy density (E) defined by the following equation [46]:

$$E = \frac{P}{v \cdot h_d \cdot t} \quad (4)$$

Where v, h_d, and t are the scanning speed, hatching distance and layer thickness respectively.

The factors A, α, and h_m can be considered constant in the construction of all samples as these are produced in the same build job with the same copper powder under the same condition. Furthermore, the size of the laser beam radius can also be considered constant as it depends on the hardware of the machine used to produce the samples. Therefore, Eq. (3) can be simplified to:

$$\frac{\Delta H}{h_m} \propto \frac{P}{\sqrt{v}} \quad (5)$$

This simplification also arises from the consideration that in reality some of the factors constantly change during the laser melting process and it is not currently possible to have an exact measurement. For example, the absorptivity of copper powder cannot be easily evaluated, due to the very condition of the process. In fact, the powder is typically sieved and reused, and even if there is a flow of inert gas in the chamber, some oxidation occurs, since the process does not occur in vacuum and the quantity of oxygen in the protective gas is not zero. Oxidation, as demonstrated in the literature [47], increases the absorptivity of copper in the infrared.

The comparison between Eqs. (4) and (5) shows an important difference between E and ΔH, even if they have the same unit of measurement (J/mm^3) and indicate the same quantity. In fact, there is a different dependance from the scanning speed (considering constant h_d and t in Eq. (4)), that is one of the quantities typically used to identify the parameter window in PBF-LB/M technology. Some studies on copper [39] have confirmed what had already been highlighted several times in the literature [43,48,49]: volumetric density energy concept cannot explain the trend of the density of the parts. As pointed out by Bertoli et al. [49], the track depth increases with the volumetric energy density, and at constant E, deeper penetration is achieved with higher laser power. This means that at least one of the parameters determining E has a greater influence on the melt pool depth than the others. The E therefore does not capture the transition between the conduction mode and the keyhole mode. According to Eagar and Tsai [50], the peak temperature reached by a material heated by a Gaussian laser heat source is proportional to the ratio $P/v^{1/2}$, so an increase in laser power has a stronger effect on the melting regime than a decrease in scan speed. This explains why the keyhole melting regime is more prevalent at higher laser powers than at lower powers.

2.2. Single scans and samples

The first tests were conducted by creating single scans (8 mm x 0.2 mm) on copper disks on which copper powder was deposited (Fig. 2a). To make the difference in microstructure between the substrate and the single scan more evident, the disks were treated at 600 °C and then slowly cooled. The surface, which was found to be oxidized, was then polished with 2400 grit sandpaper. The discs were placed inside a specially modified built platform so that the recoater blade could be used to evenly distribute the layer on the discs. It was decided to use copper discs to better simulate the powder spreading and layer-by-layer remelting effect during the construction of the cubes. In fact, during the production of a sample, the powder is spread on the previous layer rapidly solidified surface, that has a certain surface roughness. The presence of powder increases the effective absorption [51]. The importance of the surface roughness on the powder spreading was also validated since, with the same parameters, the discs with a rough surface had a better behavior than the polished discs. A series of single 10 mm long traces was produced by varying the laser power and scanning speed. In the calculation of normalised enthalpy (Eq. (3)), A, α, k and r were approximated as constant with 0.5 [51], 1.13 m^2/s [52], 330 W/mK [39] and about 50 μm respectively.

The choice of process parameters was based on the ranges of laser power and scanning speed present in the literature: laser powers from 350 to 400 W and scanning speeds from 400 to 1000 mm/s. A 30 μm layer was used. High purity argon was flowed into the build chamber to ensure low oxygen content (≤0.1 % oxygen). This gas flow serves primarily to maintain the inert atmosphere required during processing. It also has the secondary function of removing from the laser path any by-products of the process, such as vaporised powder (condensation), which could affect the characteristics of the laser beam (energy, spot diameter or intensity profile) on the powder bed. If the oxygen level in the chamber increases by approximately 0.12–0.14 % during construction, the oxygen sensors send a signal and the build chamber is filled again with inert gas.

Once the parameters allowing the best melting were identified, the melt pool depth and width values (Fig. 2b) were evaluated with an optical microscope to identify the actual layer thickness and hatching distance values. These were then used to produce samples (cubes with 10 mm side) for density analysis. For each set of parameters, three cubes were created and placed in different areas of the construction platform. The samples with the best density were replicated three more times to further verify the result obtained. In the production of cubes, a steel (SS316) building platform is used, heated at 80 °C. The same process atmosphere conditions were used for the cubes as for the single-track experiments. A metal blade in SS316L was used to spread the powder on the platform. The cubes were produced using 5mm wide stripe with bidirectional laser motion and 67° of hatch angle rotation. The choice of

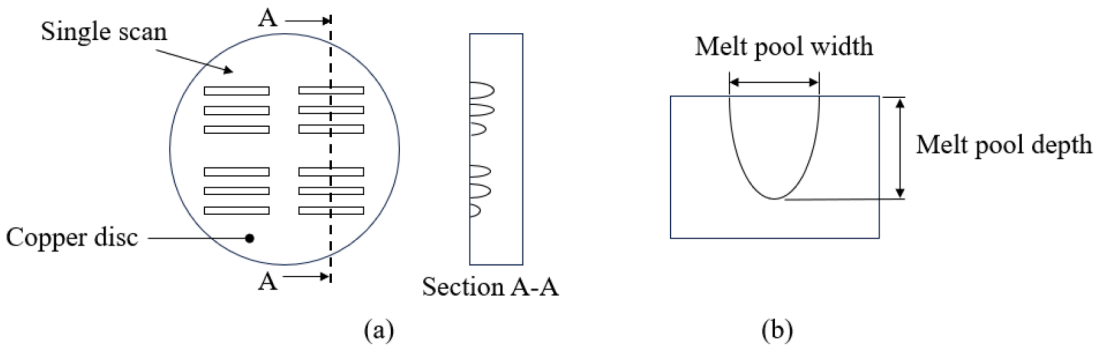

Fig. 2. Schematic illustration of (a) single scans on copper substrate and cross-section for optical microscope; (b) values used to choose the layer thickness and hatching distance.

67° is widely discussed in the literature as one of best strategy for reducing internal stresses and increasing density. Multiple studies have shown that patterns with shorter scan lengths, such as the island scan strategy, result in faster cooling and different residual stress states, especially around the sample edges [53–57]. The 67 prime number achieves the maximum variance in the 360 number space and has an optimum spacing between the angles.

2.3. Pure copper powder

Gas-atomized pure Cu powder from EOS GmbH (Fig. 3) was used. The particle size of powder ranged from 15 to 53 μm. The chemical composition according to the manufacturer's data sheet is given in Table 1.

Table 1
Powder chemical composition (wt.-%).

Element	Min.	Max.
Cu	Balance	
O	–	0.35
Other elements total	–	0.5

2.4. PBF-LB/M experiments

To produce PBF-LB/M/Cu (acronym according to ISO/ASTM 59201) single scans, a Print Sharp 250 equipped with a 500 W Yb-fiber laser (wavelength at λ = 1060–1080 nm) and a beam-spot size of 100 μm was used. This machine, named in this study M1, was chosen because the laser power is comparable to that of literature studies on pure copper produced with infrared lasers. The copper powder was spread manually using a custom recoating blade as a single layer of 30 μm on pure copper circular discs. The samples were produced using two different machines, the M1 used for single scans and the EOSINT M270 Dual Mode, referred to in this study as the M2. The M2 machine is equipped with a 200 W Yb-fiber laser (wavelength at λ = 1060–1100 nm) and a beam-spot size of 100 μm, In addition to maximum laser power, the two machines differ in term of gas flow direction and other hardware elements (control over the forces impacting the blade, etc.). They also differ in terms of the software used to manage various process parameters, including powder dosing on the build platform. As indicated in the literature [58], different machines can give different results for the same process parameters or energy density values. Therefore, in order to verify the goodness of the results obtained on cubes with the M1 machine, the best range of normalised enthalpy values were used on the M2.

2.4. Materials characterization

The density of the cubes was measured by three approaches: the Archimedes' principle with an analytical balance (KERN ABJ 320-4NM), the CT-scan (GE Phoenix v|tome|x s) and optical microscope. According to Archimedes' principle, the measurements were repeated three times for all the samples tested both in air and in distilled water. The process parameters used for the CT-scans were a voltage of 180 kV, a current of 150 μA, and a voxel size of 26.5 μm. The analyses were performed using the VGStudio Max 3.4 software. The samples that underwent microstructural investigation were obtained by cutting along the building direction and mechanical polishing using SiC papers (up to 4000 grit size) and diamond suspensions (down to 1 μm). The surfaces were etched using an ammonia/hydrogen peroxide etchant and/or a ferric chloride-based solution. The optical microstructure was observed by

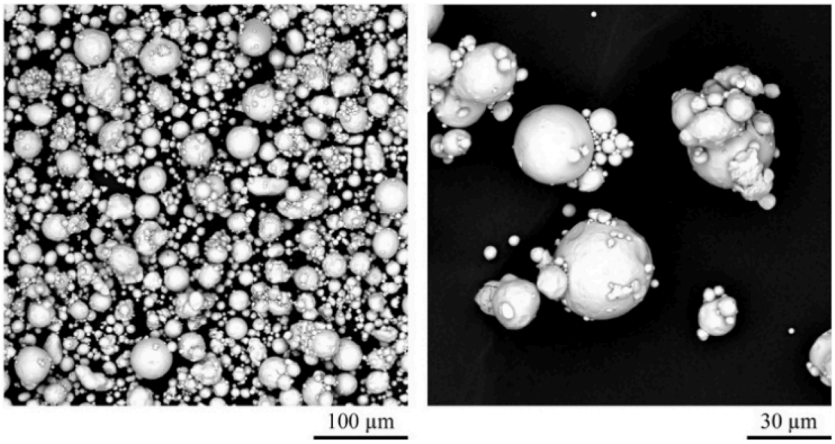

Fig. 3. Morphology of copper powder.

means of a Leica DMI5000M microscope.

3. Results and discussion

3.1. Single scans

The need to polish the disc surface to remove oxidation led to problems of increased reflection. As can be seen from Fig. 4, for the same parameters the track has a different morphology between the untreated and unpolished disc and the treated and polished one. During melting, the fumes, together with the flow of inert gas, create a certain turbulence in the fusion area, that tends to displace the powder in the fusion zone causing the laser to meet the substrate. The rectified substrate has a greater reflectivity therefore reducing absorption.

Table 2 reports the values of the $P/v^{1/2}$ from Eq. (5) for the chosen range of scanning speed and laser power. Single scans of some of these combinations were constructed to understand if there is a value or range of values that produce the desired keyhole condition (Fig. 1b). The value in bold (16.330 W $mm^{-1/2}$ $s^{1/2}$) indicates the value corresponding to the P/v ratio which according to Jadhav et al. [39] represents the transition point to the keyhole condition.

The sample representing the transition level and the one with a value of 17.500 W $mm^{-1/2}$ $s^{1/2}$ were also produced. The tracks produced in both cases were not continuous and had a high amount of spatter around the track. From the analysis of the single scans, some of which are shown in Fig. 5, it was seen that for each laser power there is a scanning speed for which the melt pool is well defined. As this scanning speed decreases or increases, the melt pool becomes wider and lower or narrower and higher. However, the parameters that generally allow to obtain the best condition are those for which the $P/v^{1/2}$ value is between approximately 13.3 and 13.7 W $mm^{-1/2}$ $s^{1/2}$.

In Eq. (5) if the laser beam radius is not considered constant, it is possible to compare the obtained values with the literature using the formula $P/(v^{1/2}.r^{3/2})$. Table 3 shows the comparison between the values indicated in the Jadhav et al. [39] study as the transition point (L1_R) and the best values of laser powder and scanning speed for the density (L2_R).

In L1_S and L2_S the diameters of this study were used. In L3_S the laser power and scanning speed values that created a continuous trace are indicated. In L3_R the diameter of this study was replaced with the one used in L1_R. The formula $P/(v^{1/2}.r^{3/2})$ used highlights, as it happens when considering the I, the important effect of the size of the laser beam. If a high amount of energy is deposited on a single track, in the construction of an area section where the hatching distance intervenes, this will be further amplified due to the partial overlapping of the tracks. This comparison confirms the difficulties encountered in building the tracks with the literature parameters having a larger diameter.

From the analysis of melt pools which present values between approximately 13.3 and 13.7 W $mm^{-1/2}$ $s^{1/2}$, the layer thickness and the hatching distance were obtained from the height and width of the melt pool respectively (Fig. 6). Multiple measurements were taken along various points of the track and averaged (Fig. 6a). A metallographic etching with ammonium hydroxide with water and hydrogen peroxide was used to identify the microstructure and therefore the penetration state of the track to obtain the layer thickness. As can be seen from Fig. 6b, some parameters did not allow to obtain a fusion between the powder and the substrate.

3.2. Cubic samples

3.2.1. M1 machine

The transition from a single scan to multiple scan tracks in plane and height results in changes in the thermal energy level due to the hatching distance and layer thickness. The hatching distance has a major impact on the overlap between adjacent scan tracks and the densification behaviour of the parts, as it significantly influences the thermal behaviour within the melt pool and consequently the melting mode and performance. In the first phase of the study, in order to better understand the changes in the process parameters to be made due to the thermal change in the transition from single scans to monolithic parts, it was decided to build the cubes using the same layer thickness deposited for each single scan and the hatching distance starting from the average value that best matched the width of the best track obtained. Cubic samples were then produced with a layer thickness of 30 μm and a hatch distance of 60 μm. However, due to the thermal effects that the hatch distance can generate, samples were produced not only with the laser power and scan speed parameters in the rage of 13.3–13.7 W $mm^{-1/2}$ $s^{1/2}$, but also in the range of 12.8 to 15.1 W $mm^{-1/2}$ $s^{1/2}$. Fig. 7 shows the results.

The sample indicated in bold in Table 2 was still produced even though the single scan did not give good results for evaluating the effect of hatching distance and layer overlap. Unfortunately, it was blocked during construction due to errors caused by spatters confirming an excess of energy. By observing the data, it is possible to confirm the range obtained from the single scans. The differences arise from the fact that an average hatching distance value was used. Therefore, based on scanning speed and laser power, this value should be gradually modified to find the most suitable one for each value. It is interesting to note that samples produced with 13.0–13.1 W $mm^{-1/2}$ $s^{1/2}$, 13.4–13.5 W $mm^{-1/2}$ $s^{1/2}$ and 13.8–13.9 W $mm^{-1/2}$ $s^{1/2}$ obtained similar results. This highlights that the values of 380 W and 390 W of laser power combined with the scanning speeds of 800 mm/s and 850 mm/s, regardless of the combination, generate a density of 93.73 % ± 0.1. So, the difference will not be perceptible at the density level but on the type and distribution of internal porosity.

Analysing the samples first visually and then by CT-scan, it emerged that they showed the presence of defects (dross formation) and larger pores on the left side (Fig. 8a). In order therefore to better understand this defect, the samples were produced with the scan vectors aligned only along the x-direction and the y-direction (Fig. 8b).

During the production of the samples, those with a scan vector along y-direction collapsed. This is due to the direction of the inert gas flow inside the chamber. The flow system consists of two inlet nozzles at the rear of the chamber and one outlet nozzle at the front. The bottom inlet nozzle establishes an almost laminar flow through the powder bed. The second upper inlet nozzle creates a flow that forces the first laminar flow towards the platform. The exit nozzle is located on the opposite side of the process table. Many researchers have studied the impact of inert gas flow on part quality and spatter behaviour [59–63]. The spatter distribution is closely linked to the direction of the gas flow, since the spatter accumulates preferentially downstream of the gas flow. Thus, the spatters should be mainly distributed along the y-direction in this study. However, the influence of the gas flow can also change the spatter distribution when scanning perpendicular to the gas flow, resulting in the presence of spatter on the powder bed along the y-direction as also

Fig. 4. Depositions on pure copper disk (a) untreated and unpolished, (b) treated and polished. Laser power 350 W.

Table 2
Power to square root of scanning speed ratio (from Eq. (5)) $P/v^{1/2}$ [W mm$^{-1/2}$ s$^{1/2}$]. The tested combinations are grey.

v [mm/s]	*P* [W]										
	350	**355**	**360**	**365**	**370**	**375**	**380**	**385**	**390**	**395**	**400**
400	17.500	17.750	18.000	18.250	18.500	18.750	19.000	19.250	19.500	19.750	20.000
450	16.499	16.735	16.971	17.206	17.442	17.678	17.913	18.149	18.385	18.620	18.856
500	15.652	15.876	16.100	16.323	16.547	16.771	16.994	17.218	17.441	17.665	17.889
550	14.924	15.137	15.350	15.564	15.777	15.990	16.203	16.416	16.630	16.843	17.056
600	14.289	14.493	14.697	14.901	15.105	15.309	15.513	15.718	15.922	16.126	**16.330**
650	13.728	13.924	14.120	14.316	14.513	14.709	14.905	15.101	15.297	15.493	15.689
700	13.229	13.418	13.607	13.796	13.985	14.174	14.363	14.552	14.741	14.930	15.119
750	12.780	12.963	13.145	13.328	13.510	13.693	13.876	14.058	14.241	14.423	14.606
800	12.374	12.551	12.728	12.905	13.081	13.258	13.435	13.612	13.789	13.965	14.142
850	12.005	12.176	12.348	12.519	12.691	12.862	13.034	13.205	13.377	13.548	13.720
900	11.667	11.833	12.000	12.167	12.333	12.500	12.667	12.833	13.000	13.167	13.333
950	11.355	11.518	11.680	11.842	12.004	12.167	12.329	12.491	12.653	12.815	12.978
1000	11.068	11.226	11.384	11.542	11.700	11.859	12.017	12.175	12.333	12.491	12.649

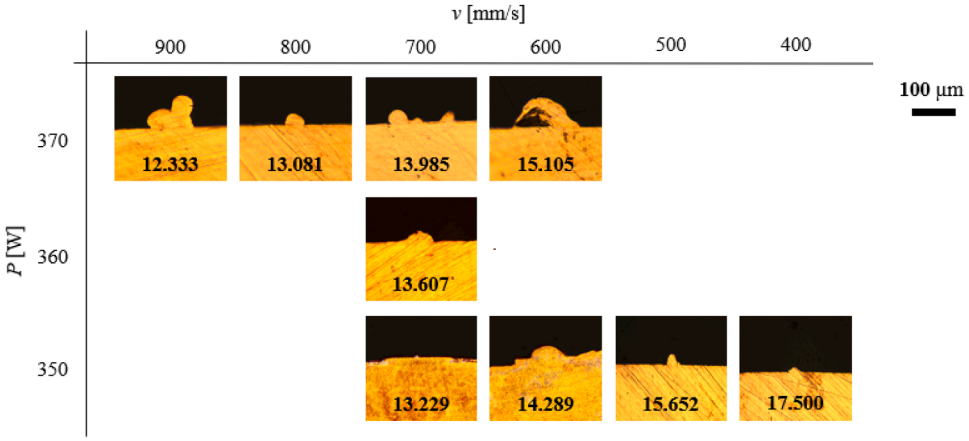

Fig. 5. Some single scans with the respective value of $P/v^{1/2}$.

Table 3
Comparison with the literature.

	P [W]	*v* [mm/s]	*d* [mm]	*I* [kW/mm^2]	*P/v* [W/mm·s^{-1}]	$P/v^{1/2}$ [W mm^{-2} s$^{1/2}$]	$P/(v^{1/2}\cdot r^{3/2})$ [W mm^{-2} s$^{1/2}$]
L1_R	400	600	0.0375	362.166	0.667	16.330	6360.371
L1_S	400	600	0.100	50.930	0.667	16.330	1460.593
L2_R	500	800	0.0375	452.707	0.625	17.678	6885.304
L2_S	500	800	0.100	63.662	0.625	17.678	1581.139
L3_S	370	800	0.100	47.110	0.463	13.081	1170.043
L3_R	370	800	0.0375	335.003	0.463	13.081	5095.125

highlighted by Liu et al. [64]. Moreover, with adequate laser power density, droplet spatters tend to be ejected in the direction opposite to the scanning direction [65], which explains the enrichment of spatters detected in the side regions during the *x*-direction scanning strategy. Therefore, in the 67° scanning strategy, when the scanning direction coincides, albeit with differences of a few degrees, with the *y*-direction, the layer appears to be defective and the spatters that are created tend to settle in certain areas producing the defects. To overcome this problem, it is possible to insert a hatch angle and/or change the direction of the scanning strategy from bidirectional to unidirectional by scanning against the flow. If a hatch angle is entered, hatch lines against the flow or with an angle less than half the hatch angle will be skipped. If flow optimisation is also activated, the exposure starts from the hatch line furthest from the flow inlet and the overlapping blade and the strip exposure changes from bi-directional to uni-directional. To overcome this problem, some manufacturers allow the scanning strategy to be changed by entering a restriction angle and/or a flow optimization changing the direction of the scanning strategy from bidirectional to unidirectional when at angles close to the *y*-direction (Fig. 9). If a

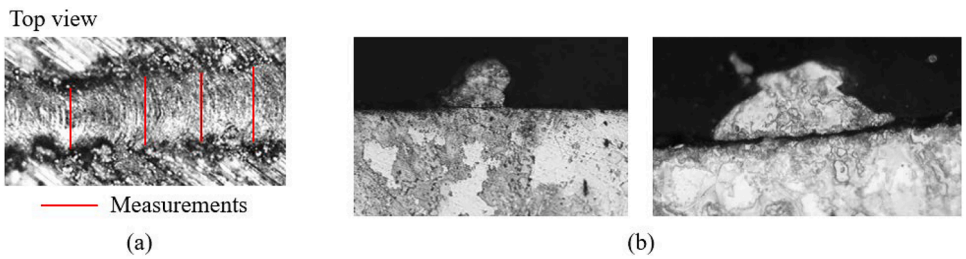

Fig. 6. Example of the measure of the (a) hatching distance; (b) metallographic attack on a section of the track which highlights the non-penetration into the substrate.

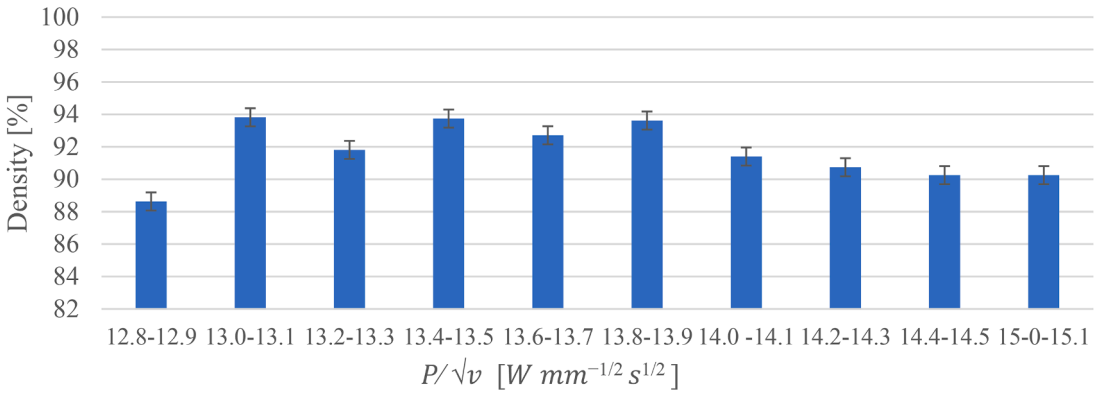

Fig. 7. Density measured by Archimedes' method. Samples produced by Print Sharp 250 machine.

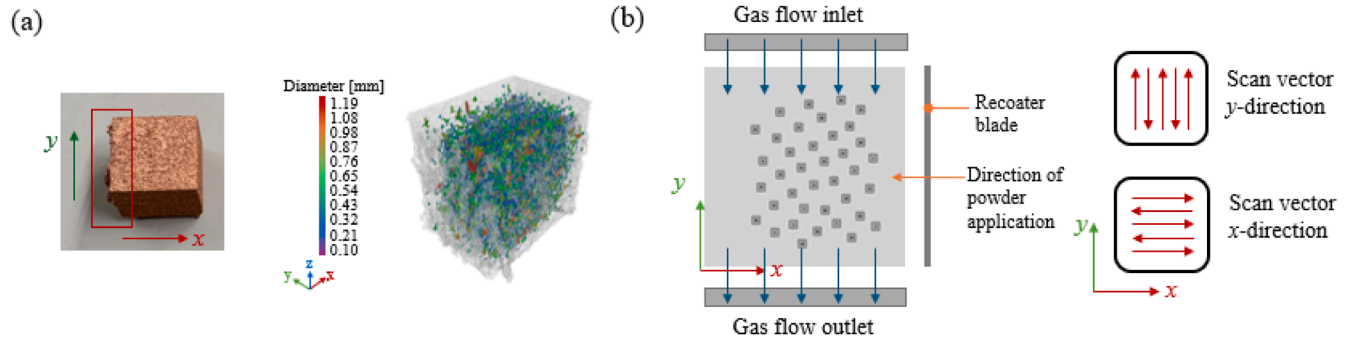

Fig. 8. (a) Example of defects on the samples (red rectangle); (b) placement in the inlet piping and scanning strategy.

restriction angle is entered (Fig. 9b), hatch lines against the flow or in an angle smaller than half the restriction angle will be skipped. If flow optimization is enabled, the exposure starts at the most distant hatch line from the flow inlet and the recoater blade and the exposure of stripe will change from bidirectional to unidirectional (Fig. 9c).

3.2.2. M2 machine

Starting from the results obtained with the machine M1, it was decided to produce the samples also on a machine with a 200W laser to verify whether, regardless of the manufacturer and model of the PBF-LB/M machine used, the results were confirmed and to verify the effect of the inert gas flow. Also in this case, some process parameters combinations representatives of the previously tested range were chosen. Neither the hatching distance nor the layer thickness were changed. Table 3 shows the results. The trend of density versus $P/v^{1/2}$ ratio was confirmed and the results regarding the density and defects of both internal and external surfaces were improved. The E1 sample was interrupted during construction since it showed defects due to an excess of energy which could lead to black reflection of the laser. All the samples were polished and observed at the optical microscope. It was observed that the internal structure not always corresponded to the Archimedes observation. In particular, the external surface of the cubes could have a much lower porosity than the internal one, possibly due to the increased heat dissipation from the internal layers with respect to the external ones. Samples E4, E6 and E7 were very porous in the inner part, while a stitching of 30 optical microscopy images of samples 2, 3 and 5, shown in Fig. 10, gave the porosity indicated in Table 4. What emerges from the observation of these samples, and which is also highlighted in Fig. 10 for sample E3, is the presence of denser and less dense areas. This may also be due to the inhomogeneous oxidation of the powder. Each time the powder is reused, the percentage of oxygen increases. As highlighted by Yang et al. [66], the more the oxygen content

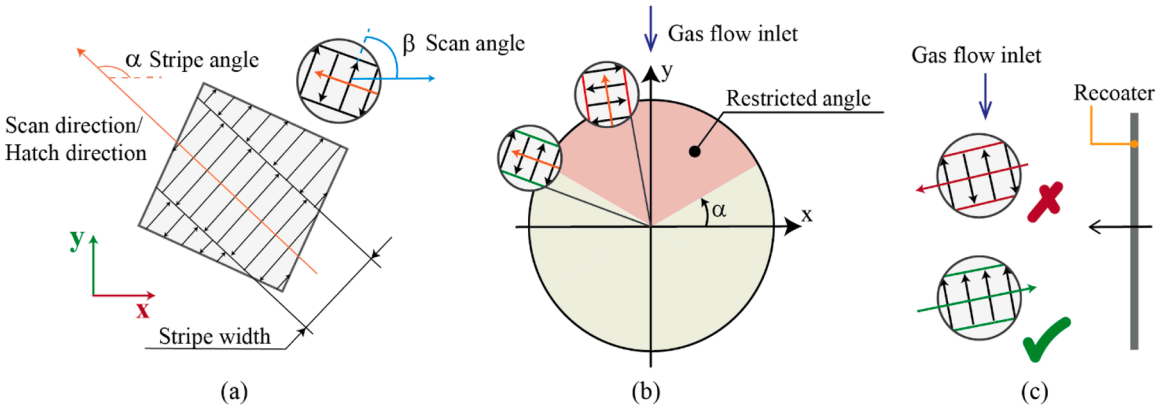

Fig. 9. (a) Relation between stripe width, scan angle and hatch direction; (b) illustration of the restriction angle; (c) flow optimization.

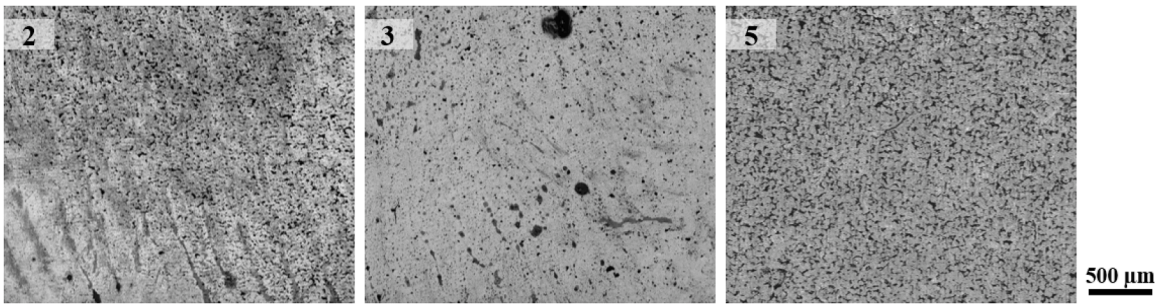

Fig. 10. Optical microscope images of samples E2, E3, and E5.

Table 4
Process parameters used to produce samples and relative density. Samples produced by EOSINT M270 Dual Mode machine.

Samples	P [W]	v [mm/s]	$P/v^{1/2}$ [W mm$^{-1/2}$ s$^{1/2}$]	Density [%]		
				Archimedes	Optical	Ct-scan
E1	185	110	17.639	–	–	–
E2	185	180	13.789	94.42 ± 0.74	90.4	98.77
E3	185	190	13.421	93.93 ± 0.83	96.7	98.79
E4	185	220	12.473	93.87 ± 0.35	very porous	
E5	190	210	13.111	94.47 ± 0.25	84.1	
E6	190	220	12.810	94.23 ± 0.28	very porous	
E7	195	190	14.147	94.08 ± 0.31	very porous	

in the powder increases, the more the percentage of porosity is reduced by increasing the density up to over 99 % with the same process parameters. If the powder is voluntarily oxidised to create a uniform film, the result of the density and porosity present will be uniformly distributed, otherwise there may be areas of higher density and porous areas on the same sample. Samples E2 and E3 were also analysed by CT-scan to verify that the measured density was indeed high (Fig. 10).

These results raise some issue about the measuring methods of porosity. It is generally known in the literature that these three different porosity measurement methods lead to slightly different results due to the different measurement method [67–71]. Each of these methods has advantages and disadvantages but what is interesting is the different information they can provide, and which allows an analysis from multiple points of view. Archimedes method gives the apparent density, not considering the porosity accessible from the outside, while Ct-scan does not give information on porosity significantly smaller than the voxel size. Porosity calculated by optical methods can give false information when the porosity distribution is not homogeneous in the volume of the sample. For instance, in sample E5 two different porosity results were obtained when polishing a plane passing in the centre of the sample or on the surface.

In this case, for sample E3, the results obtained from all three methods used for density measurement are significantly higher than most of the articles in the literature on pure copper, which state the difficulty if not the impossibility of obtaining densities higher than 95 % using infrared lasers with powers lower than 200 W [72]. If only the $P/v^{1/2}$ ratio is considered, the best results belong to the same ranges (13.4–13.5 W mm$^{-1/2}$ s$^{1/2}$) on both the Print Sharp 250 and the EOSINT M270. However, looking at the CT scan image of the sample with the same $P/v^{1/2}$ ratio (Fig. 11) a difference in pore diameters can be noticed between two machines. An explanation can be found in the inert gas path inside the machines that is different in the two cases. This effect could make the effects on the samples more homogeneous regardless of the position on the platform and the rotation of the vectors on a layer with respect to the flow direction. In fact, the gas in the EOSINT M270 enters the chamber from the top right. Toroidal vortices are created that surround the hot vertical jet of metallic vapor. These vortices remain unchanged near a laser spot throughout the fusion process, forming a recirculation zone around the heat-affected region. As highlighted by Noskov et al. [73], nanometer-sized particles, due to their mass, will exactly follow the flow lines of the gas, eventually becoming trapped in the toroidal vortices. Subsequently these particles grow and move towards the peripheral regions of the vortex, and then abandon it. The right choice of gas flow rate, even more so in the case of lamellar flow as in the Print Sharp 250, can lead to effective removal of airborne particles outside the processing zone, preventing their reflow into a circulating toroidal vortex of the carrier gas.

3.2.3. *Effect of the hatching distance and stripe*

In the transition from single scans to cubes, in addition to laser power and scanning speed, other factors intervene such as the layer thickness, the hatching distance, the size of the stripes and their overlap, the contour, etc. These factors are not included in the deposited energy density as it has been proposed in the laser welding field [74]. As highlighted by Kunieda et al. [74] this index should be modified by inserting the hatching distance to be more suitable for the PBF-LB/M process and they propose the use of $P/(v^{1/2}{\cdot}h_d{}^{1/2})$. Starting from the two best samples (E2 and E3) the hatching distance was varied to verify the behaviour (Table 5).

Reducing the h_d by 0.01 mm led to a 1 % density reduction with an increase in spherical porosity while increasing by 0.01 mm led to the formation of lack of fusion defects. As a results, the optimized laser condition for this study is in the range of $P/(v^{1/2}{\cdot}h_d{}^{1/2})$ = 54.8–56.3 W·mm^{-2}·s$^{1/2}$. Since other factors that intervene in the process must also be taken into account, the effect of stripe reduction was analyzed. Reducing the strip width from 5 mm to 3 mm did not lead to significant improvements in density and reduction of spherical porosity. Reducing the strip overlap by 0.02 mm did not lead to any significant changes, except for a very slight deterioration.

Comparing with the literature for the realization of dense pure copper specimens by the PBF-LB/M process, it can be seen that the difference between R1 [39] and R2 [75] for E is about 10 % despite the dimensions of the laser diameter are very different (for R1 the diameter is 0.0375 mm, for R2 the diameter is 0.100 mm) which has been seen to have a certain weight. If the comparison is made with the index proposed in the literature, the difference increases by about 27 %. It can therefore be stated that both at the level of single scans and cubes, the deposited energy density gives indications more relevant to the process. When changing the hatching distance, it is necessary to consider the effects not only of the optical spot size but also of the effective spot size, i.e. the powder fusion region. The powder layer is not constant on each previously spread layer due to the effect of the blade passage and this therefore makes it difficult to realistically describe the effect of each process parameter through indices. The powder will be higher at the

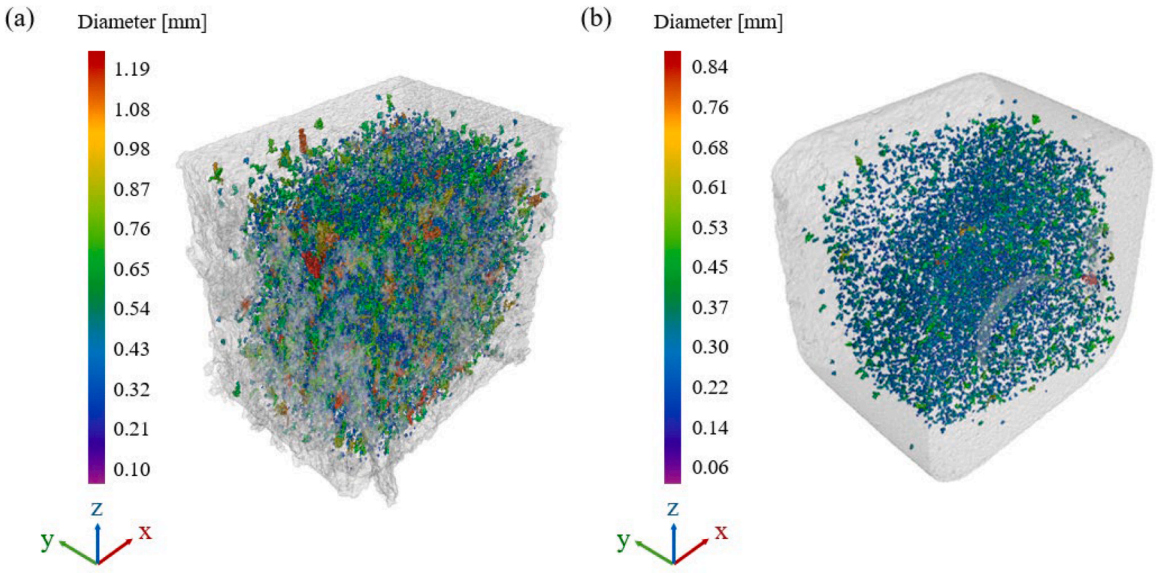

Fig. 11. Ct-scan of the sample with the same $P/v^{1/2}$ ratio produced with the machines (a) M1 and (b) M2.

Table 5
h_d values used and process index proposed by Kunieda et al. [74] compared with the energy density. To better compare the indices and taking into account that the layer thickness is constant, this has not been calculated in the energy density.

Samples	P [W]	v [mm/s]	h_d [mm]	$P/\sqrt{v \cdot h_d}$ [W·mm^{-2}·s$^{1/2}$]	E [J/mm^2]
E2	185	180	0.06	56.294	17.130
E3	185	190	0.06	54.792	16.228
H1	185	180	0.05	61.667	20.556
H2	185	190	0.05	60.022	19.474
H3	185	180	0.07	52.118	14.683
H4	185	190	0.07	50.728	13.910
R1	500	800	0.09	58.926	6.944
R2	300	600	0.08	43.301	6.250

starting point of the application and lower at the final point after coverage also based on how many samples it will encounter along the way and their different surface roughness. During the fusion, the area will tend to be lower than the powder plane due to gravity, due to its weight, and therefore, even if the platform is lowered by a given layer, the height of the layer will be different in the various areas of the powder bed. This leads to a different interaction at each layer between the powder and the laser which will affect the density and defects. This effect is visible when looking microscopically at samples along the growth *z*-section constructed with a strategy in the *xy*-plane along only the *x*- or *y*- direction, but one is unable to see the effect when a 67° strategy is used [48,76].

4. Conclusion

In this paper, the processing behavior of laser-based powder bed fusion of pure copper powder was evaluated using an infrared fiber laser with two different machines having different maximum laser power 500 W and 200 W. On the basis of the results, the following conclusions have been drawn:

- Normalised enthalpy is used instead of volumetric energy density to enable the production of parts with the PBF-LB/M additive process for highly reflective materials. The normalised enthalpy allows the process parameter ranges corresponding to the different melting modes (conduction, transition, keyhole and balling) to be determined more correctly.
- Two machines with different hardware and software elements were used to verify the quality of the results obtained. The optimized laser condition is in the range of $P/(v^{1/2} \cdot h_d^{1/2}) = 54.8–56.3$ W·mm^{-2}·s$^{1/2}$. Considering only the $P/v^{1/2}$ ratio, the best results belong to the same ranges, 13.4–13.5 W·mm^{-2}·s$^{1/2}$, for both PBF-LB/M machines used.
- Laser power of 185 W has been shown to be sufficient for the fabrication of bulk solid copper parts with density greater than 94 % by Archimedes' method and 98 % analyzed by CT and optical analysis.
- This investigation demonstrates that high density solid copper bulk components can be successfully produced using an infrared fiber laser with 185 W laser power, provided that the PBF-LB/M settings used are sufficient to produce keyhole melting to increase the absorptivity.
- In order to reproduce the satisfactory results obtained on a PBF-LB/M machine on another system, it is not enough to simply consider the energy values, but it is necessary to analyse the differences between the machines and understand how to ensure that these do not compromise the result. In the case of lamellar gas flow on the build platform, it is important to understand which is the best scanning strategy to use in order to reduce the negative effects of the laser direction compared to the gas direction.
- Although the deposited energy density provides the bounds of the laser conditions for the fabrication of dense highly reflective materials, it must be modified to account for the effect of other process parameters such as hatching distance.

CRediT authorship contribution statement

Flaviana Calignano: Writing – original draft, Validation, Supervision, Methodology, Investigation, Formal analysis, Conceptualization. **Alessandro Bove:** Validation, Formal analysis. **Matteo Pavese:** Writing – original draft, Validation, Investigation, Formal analysis.

Declaration of competing interest

The authors declare that they have no known competing financial interests or personal relationships that could have appeared to influence the work reported in this paper.

Data availability

No data was used for the research described in the article.

References

[1] C. Semini, J. Goldsmith, D. Manfredi, F. Calignano, E.P. Ambrosio, J. Pakkanen, D. G. Caldwell, Additive manufacturing for agile legged robots with hydraulic actuation, in: In: Proceedings of the 17th International Conference on Advanced Robotics, ICAR, 2015, p. 2015, https://doi.org/10.1109/ICAR.2015.7251444.

[2] O.A. Peverini, G. Addamo, M. Lumia, G. Virone, F. Calignano, M. Lorusso, D. Manfredi, Additive manufacturing of ku/K-band waveguide filters: a comparative analysis among selective-laser melting and stereolithography, IET Microw., Antenn. Propag. 11 (14) (2017) 1936–1942, https://doi.org/10.1049/iet-map.2017.0151.

[3] W. Associates, Wohlers Report 2020: 3D Printing and Additive Manufacturing Global State of the Industry, Wohlers Assoc. Inc, 2020.

[4] C.Y. Yap, C.K. Chua, Z.L. Dong, Z.H. Liu, D.Q. Zhang, L.E. Loh, S.L. Sing, Review of selective laser melting: materials and applications, Appl. Phys. Rev. 2 (4) (2015) 041101, https://doi.org/10.1063/1.4935926.

[5] J. Zhou, R.A. Barrett, S.B. Leen, Three-dimensional finite element modelling for additive manufacturing of Ti-6Al-4V components: effect of scanning strategies on temperature history and residual stress, J. Adv. Join. Process. 5 (2022) 100106, https://doi.org/10.1016/j.jajp.2022.100106.

[6] T. Tom, S.P. Sreenilayam, D. Brabazon, J.P. Jose, B. Joseph, K. Madanan, S. Thomas, Additive manufacturing in the biomedical field-recent research developments, Results Eng. 16 (2022) 100661, https://doi.org/10.1016/j.rineng.2022.100661.

[7] A.A. Akinwande, O.A. Balogun, A.A. Adediran, O.S. Adesina, V. Romanovski, T. C. Jen, Experimental analysis, statistical modeling, and parametric optimization of quinary-(CoCrFeMnNi)100 –x/TiCx high-entropy-alloy (HEA) manufactured by laser additive manufacturing, Results Eng. 17 (2023) 100802, https://doi.org/10.1016/j.rineng.2022.100802.

[8] T. Newswander, R.A. Paquin, Materials for optical systems. Handbook of Optomechanical Engineering, Second Edition, 2017, p. 38, https://doi.org/10.4324/9781315153247.

[9] C. Keller, Processing of highly reflective materials, Laser Tech. 4 (2017) 30–33, https://doi.org/10.1002/latj.201700024.

[10] S.D. Jadhav, S. Dadbakhsh, L. Goossens, J.P. Kruth, J. Van Humbeeck, K. Vanmeensel, Influence of selective laser melting process parameters on texture evolution in pure copper, J. Mater. Process. Technol. 270 (2019) 47–58, https://doi.org/10.1016/j.jmatprotec.2019.02.022.

[11] S. Zhang, H. Zhu, Z. Hu, X. Zeng, F. Zhong, Selective laser melting of Cu–10Zn alloy powder using high laser power, Powder Technol. 342 (2019) 613–620, https://doi.org/10.1016/j.powtec.2018.10.002.

[12] D.Q. Zhang, Z.H. Liu, C.K. Chua, Investigation on forming process of copper alloys via selective laser melting, in: In: Proceedings of the 6th International Conference Advanced Research on Rapid Prototyping, 2014, https://doi.org/10.1201/b15961-53. VR@P 2013.

[13] T. Gustmann, H. Schwab, U. Kühn, S. Pauly, Selective laser remelting of an additively manufactured Cu–Al–Ni–Mn shape-memory alloy, Mater. Des. 153 (2018) 129–138, https://doi.org/10.1016/j.matdes.2018.05.010.

[14] J. Tian, W. Zhu, Q. Wei, S. Wen, S. Li, B. Song, Y. Shi, Process optimization, microstructures and mechanical properties of a Cu-based shape memory alloy fabricated by selective laser melting, J. Alloys Compd. (2019), https://doi.org/10.1016/j.jallcom.2019.01.153.

[15] M. Sinico, G. Cogo, M. Benettoni, I. Calliari, A. Pepato, Influence of powder particle size distribution on the printability of pure copper for selective laser melting, in: In: 2019 Proceedings of the 30th Annual International Solid Freeform Fabrication Symposium - An Additive Manufacturing Conference SFF 2019, 2019.

[16] S. Gruber, L. Stepien, E. López, F. Brueckner, C. Leyens, Physical and geometrical properties of additively manufactured pure copper samples using a green laser source, Materials (Basel) 14 (13) (2021) 3642, https://doi.org/10.3390/ma14133642.

[17] M. Horn, M. Schmitt, M. Schafnitzel, A. van Husen, P. Wagenblast, S. Auernhammer, J. Heyder, C. Hauck, J. Barz, M. Ott, G. Schlick, C. Seidel, Powder Bed fusion of highly filigree copper features using a green laser, Proc. CIRP 11 (2022) 81–86, https://doi.org/10.1016/j.procir.2022.08.135.

[18] D. Wang, K. Li, J. Yao, B. Du, Y. Xu, Porosity, texture, and mechanical properties of pure copper fabricated by fine green laser powder bed fusion, Opt. Laser Technol. 181 (2025) 112009, https://doi.org/10.1016/J.OPTLASTEC.2024.112009.

[19] T. Romano, A. Ratkus, S. Gruber, M. Pozzi, H. Kos, C. Garion, S. Rorison, E. López, T. Torims, M. Vedani, Pure copper membranes manufactured by green laser powder bed fusion with varying wall-thickness and building orientation: microstructure, properties, and vacuum tightness performance, Vacuum 233 (2025) 113995, https://doi.org/10.1016/J.VACUUM.2024.113995.

[20] Y.H. Zhou, Z.H. Zhang, Y.P. Wang, G. Liu, S.Y. Zhou, Y.L. Li, J. Shen, M. Yan, Selective laser melting of typical metallic materials: an effective process prediction model developed by energy absorption and consumption analysis, Addit. Manuf. 25 (2019) 204–217, https://doi.org/10.1016/j.addma.2018.10.046.

[21] S.D. Jadhav, J. Vleugels, J.P. Kruth, J. Van Humbeeck, K. Vanmeensel, Mechanical and electrical properties of selective laser-melted parts produced from surface-oxidized copper powder, Mater. Des. Process. Commun. 2 (2020) 1–8.e94, https://doi.org/10.1002/mdp2.94.

[22] S.D. Jadhav, P.P. Dhekne, E. Brodu, B. Van Hooreweder, S. Dadbakhsh, J.P. Kruth, J. Van Humbeeck, K. Vanmeensel, Laser powder bed fusion additive manufacturing of highly conductive parts made of optically absorptive carburized CuCr1 powder, Mater. Des. 198 (2021) 109369, https://doi.org/10.1016/j.matdes.2020.109369.

[23] R. Fabbro, F. Coste, S. Slimani, F. Briand, Study of keyhole geometry for full penetration Nd-Yag CW laser welding, in: In: Conference on Lasers and Electro-Optics - Technical Digest, 2005, https://doi.org/10.1109/CLEOE.2005.1568435.

[24] P. De Bono, I. Metsios, J. Blackburn, P. Hilton, Laser processing of thin copper and aluminium thin sheets with green (532nm) and infrared (1064nm) pulsed laser beam sources, in: In: ICALEO, 32nd International Congress on Applications of Lasers & Electro-Optics, 2013, https://doi.org/10.2351/1.5062925.

[25] J.Y. Lee, S.H. Ko, D.F. Farson, C.D. Yoo, Mechanism of keyhole formation and stability in stationary laser welding, J. Phys. D. Appl. Phys. 35 (2002) 1570, https://doi.org/10.1088/0022-3727/35/13/320.

[26] S. Engler, R. Ramsayer, R. Poprawe, Process studies on laser welding of copper with brilliant green and infrared lasers, Phys. Procedia 12 (2011) 339–346, https://doi.org/10.1016/j.phpro.2011.03.142.

[27] W.E. King, H.D. Barth, V.M. Castillo, G.F. Gallegos, J.W. Gibbs, D.E. Hahn, C. Kamath, A.M. Rubenchik, Observation of keyhole-mode laser melting in laser powder-bed fusion additive manufacturing, J. Mater. Process. Technol. 214 (2014) 2915–2925, https://doi.org/10.1016/j.jmatprotec.2014.06.005.

[28] M. Bayat, A. Thanki, S. Mohanty, A. Witvrouw, S. Yang, J. Thorborg, N.S. Tiedje, J. H. Hattel, Keyhole-induced porosities in laser-based powder Bed Fusion (L-PBF) of Ti6Al4V: high-fidelity modelling and experimental validation, Addit. Manuf. (2019), https://doi.org/10.1016/j.addma.2019.100835.

[29] R. Cunningham, C. Zhao, N. Parab, C. Kantzos, J. Pauza, K. Fezzaa, T. Sun, A. D. Rollett, Keyhole threshold and morphology in laser melting revealed by ultrahigh-speed x-ray imaging, Science (80) (2019), https://doi.org/10.1126/science.aav4687.

[30] S.A. Khairallah, A.T. Anderson, A. Rubenchik, W.E. King, Laser powder-bed fusion additive manufacturing: physics of complex melt flow and formation mechanisms of pores, spatter, and denudation zones, Acta Mater. (2016), https://doi.org/10.1016/j.actamat.2016.02.014.

[31] L.J. Zhang, G.F. Zhang, J. Ning, X.J. Zhang, J.X. Zhang, Microstructure and properties of the laser butt welded 1.5-mm thick T2 copper joint achieved at high welding speed, Mater. Des. 108 (2015) 36–45, https://doi.org/10.1016/j.matdes.2015.09.072.

[32] M. Balbaa, S. Mekhiel, M. Elbestawi, J. McIsaac, On selective laser melting of Inconel 718: densification, surface roughness, and residual stresses, Mater. Des. 193 (2020) 108818, https://doi.org/10.1016/j.matdes.2020.108818.

[33] B.J. Simonds, J. Tanner, A. Artusio-Glimpse, P.A. Williams, N. Parab, C. Zhao, T. Sun, The causal relationship between melt pool geometry and energy absorption measured in real time during laser-based manufacturing, Appl. Mater. Today 23 (2021) 101049, https://doi.org/10.1016/j.apmt.2021.101049.

[34] Y.A. Mayi, M. Dal, P. Peyre, M. Bellet, R. Fabbro, Physical mechanisms of conduction-to-keyhole transition in laser welding and additive manufacturing processes, Opt. Laser Technol. (2023), https://doi.org/10.1016/j.optlastec.2022.108811.

[35] BS EN ISO 11145 : 2018 BSI Standards publication optics and photonics – Lasers and laser- related equipment – Vocabulary and symbols (2018).

[36] T. Sakai, Y. Okamoto, N. Taura, R. Saito, A. Okada, Effect of scanning speed on molten metal behaviour under angled irradiation with a continuous-wave laser, J. Mater. Process. Technol. 313 (2023) 117866, https://doi.org/10.1016/J.JMATPROTEC.2023.117866.

[37] H.J. Eichler, J. Eichler, O. Lux, Lasers Basics, Advances and applications, 2018.

[38] M.W. Sigrist, Laser: theorie, Typen und anwendungen, 2018. https://doi.org/10.1007/978-3-662-57515-4.

[39] S.D. Jadhav, L.R. Goossens, Y. Kinds, B. Van Hooreweder, K. Vanmeensel, Laser-based powder bed fusion additive manufacturing of pure copper, Addit. Manuf. 42 (2021) 101990, https://doi.org/10.1016/j.addma.2021.101990.

[40] Z.X. Ma, J. Ning, B. Yu, L.J. Zhang, J.H. Fan, L.G. Yuan, Effects of process parameters and scanning patterns on quality of thin-walled copper flanges manufactured by selective laser melting, J. Manuf. Process. 72 (2021) 419–430, https://doi.org/10.1016/j.jmapro.2021.10.042.

[41] T. Stoll, P. Trautnitz, S. Schmiedeke, J.E. Franke, N. Travitzky, Process development for laser powder bed fusion of pure copper, in: 2020. https://doi.org/10.1117/12.2563870.

[42] D.B. Hann, J. Iammi, J. Folkes, A simple methodology for predicting laser-weld properties from material and laser parameters, J. Phys. D. Appl. Phys. (2011), https://doi.org/10.1088/0022-3727/44/44/445401.

[43] A. Suzuki, R. Nishida, N. Takata, M. Kobashi, M. Kato, Design of laser parameters for selectively laser melted maraging steel based on deposited energy density, Addit. Manuf. 28 (2019) 160–168, https://doi.org/10.1016/j.addma.2019.04.018.

[44] Y. Huang, T.G. Fleming, S.J. Clark, S. Marussi, K. Fezzaa, J. Thiyagalingam, C.L. A. Leung, P.D. Lee, Keyhole fluctuation and pore formation mechanisms during laser powder bed fusion additive manufacturing, Nat. Commun. 13 (2022) 1170, https://doi.org/10.1038/s41467-022-28694-x.

[45] Z. Gan, O.L. Kafka, N. Parab, C. Zhao, L. Fang, O. Heinonen, T. Sun, W.K. Liu, Universal scaling laws of keyhole stability and porosity in 3D printing of metals, Nat. Commun. 12 (2021) 2379, https://doi.org/10.1038/s41467-021-22704-0.

[46] D. Bourell, J. Coholich, A. Chalancon, A. Bhat, Evaluation of energy density measures and validation for powder bed fusion of polyamide, CIRP Ann. - Manuf. Technol. 66 (2017) 217–220, https://doi.org/10.1016/j.cirp.2017.04.128.

[47] B. Brandau, A. Da Silva, C. Wilsnack, F. Brueckner, A.F.H. Kaplan, Absorbance study of powder conditions for laser additive manufacturing, Mater. Des. (2022), https://doi.org/10.1016/j.matdes.2022.110591.

[48] F. Calignano, G. Cattano, D. Manfredi, Manufacturing of thin wall structures in AlSi10Mg alloy by laser powder bed fusion through process parameters, J. Mater. Process. Technol. 255 (2018) 773–783, https://doi.org/10.1016/j.jmatprotec.2018.01.029.
[49] U. Scipioni Bertoli, A.J. Wolfer, M.J. Matthews, J.P.R. Delplanque, J. M. Schoenung, On the limitations of volumetric energy density as a design parameter for selective laser melting, Mater. Des. 133 (2017) 331–340, https://doi.org/10.1016/j.matdes.2016.10.037.
[50] T.W. Eagar, N.S. Tsai, Temperature fields produced by traveling distributed heat sources, Weld. J. (Miami, Fla) (1983).
[51] L. Gargalis, J. Ye, M. Strantza, A. Rubenchik, J.W. Murray, A.T. Clare, I.A. Ashcroft, R. Hague, M.J. Matthews, Determining processing behaviour of pure Cu in laser powder bed fusion using direct micro-calorimetry, J. Mater. Process. Technol. (2021), https://doi.org/10.1016/j.jmatprotec.2021.117130.
[52] J.K. Carson, M. Alsowailem, Thermal diffusivity of copper/linear-low-density polyethylene composites, Polym. Polym. Compos. (2017), https://doi.org/10.1177/096739111702500603.
[53] M.N. Doğu, S. Ozer, M.A. Yalçın, K. Davut, M.A. Obeidi, C. Simsir, H. Gu, C. Teng, D. Brabazon, A comprehensive study of the effect of scanning strategy on IN939 fabricated by powder bed fusion-laser beam, J. Mater. Res. Technol. 33 (2024) 5457–5481, https://doi.org/10.1016/J.JMRT.2024.10.171.
[54] H.L. Wei, T. Mukherjee, W. Zhang, J.S. Zuback, G.L. Knapp, A. De, T. DebRoy, Mechanistic models for additive manufacturing of metallic components, Prog. Mater. Sci. (2021), https://doi.org/10.1016/j.pmatsci.2020.100703.
[55] B. Cheng, S. Shrestha, K. Chou, Stress and deformation evaluations of scanning strategy effect in selective laser melting, Addit. Manuf. (2016), https://doi.org/10.1016/j.addma.2016.05.007.
[56] M. Strantza, R.K. Ganeriwala, B. Clausen, T.Q. Phan, L.E. Levine, D.C. Pagan, J.P. C. Ruff, W.E. King, N.S. Johnson, R.M. Martinez, V. Anghel, G. Rafailov, D. W. Brown, Effect of the scanning strategy on the formation of residual stresses in additively manufactured Ti-6Al-4V, Addit. Manuf. (2021), https://doi.org/10.1016/j.addma.2021.102003.
[57] M.A. Obeidi, Metal additive manufacturing by laser-powder bed fusion:guidelines for process optimisation, Results Eng. 15 (2022) 100473, https://doi.org/10.1016/j.rineng.2022.100473.
[58] A.M. Khorasani, I. Gibson, J.K. Veetil, A.H. Ghasemi, A review of technological improvements in laser-based powder bed fusion of metal printers, Int. J. Adv. Manuf. Technol. 108 (2020) 191–209, https://doi.org/10.1007/s00170-020-05361-3.
[59] A. Ladewig, G. Schlick, M. Fisser, V. Schulze, U. Glatzel, Influence of the shielding gas flow on the removal of process by-products in the selective laser melting process, Addit. Manuf. (2016), https://doi.org/10.1016/j.addma.2016.01.004.
[60] A.B. Anwar, Q.C. Pham, Selective laser melting of AlSi10Mg: effects of scan direction, part placement and inert gas flow velocity on tensile strength, J. Mater. Process. Technol. 240 (2017) 388–396, https://doi.org/10.1016/j.jmatprotec.2016.10.015.
[61] A.B. anwar, i.h. ibrahim, q.c. pham, Spatter transport by inert gas flow in selective laser melting: s simulation study, Powder Technol. (2019), https://doi.org/10.1016/j.powtec.2019.04.044.
[62] J. Weaver, A. Schlenoff, D. Deisenroth, S. Moylan, Assessing the influence of non-uniform gas speed on the melt pool depth in laser powder bed fusion additive manufacturing, Rapid Prototyp. J. (2023), https://doi.org/10.1108/RPJ-10-2022-0366.
[63] A.B.S. Alquaity, Influence of nozzle diameter and gas flow on spatter removal in laser powder bed fusion: a CFD approach, Results Eng. 25 (2025) 103759, https://doi.org/10.1016/J.RINENG.2024.103759.
[64] Z. Liu, Y. Yang, D. Wang, Z. Chen, W. Yan, Correlation between the scan strategy, residing spatter distribution, and parts quality in laser powder bed fusion, Mater. Des. 234 (2023) 112317, https://doi.org/10.1016/j.matdes.2023.112317.
[65] Z. Liu, Y. Yang, C. Han, H. Zhou, H. zhou, M. Wang, L. Liu, H. Wang, Y. Bai, D. Wang, Effects of gas flow parameters on droplet spatter features and dynamics during large-scale laser powder bed fusion, Mater. Des. (2023), https://doi.org/10.1016/j.matdes.2022.111534.
[66] P. Yang, D. He, S. Lu, S. Chen, D. Oleksandr, X. Guo, Influence of surface micro-oxidation on the formability of pure copper powders by selective laser melting, J. Mater. Res. Technol. (2024), https://doi.org/10.1016/j.jmrt.2024.01.026.
[67] W.W. Wits, S. Carmignato, F. Zanini, T.H.J. Vaneker, Porosity testing methods for the quality assessment of selective laser melted parts, CIRP Ann. - Manuf. Technol. (2016), https://doi.org/10.1016/j.cirp.2016.04.054.
[68] T. de Terris, O. Andreau, P. Peyre, F. Adamski, I. Koutiri, C. Gorny, C. Dupuy, Optimization and comparison of porosity rate measurement methods of Selective laser melted metallic parts, Addit. Manuf. (2019), https://doi.org/10.1016/j.addma.2019.05.035.
[69] P. Wang, X. Tan, C. He, M.L.S. Nai, R. Huang, S.B. Tor, J. Wei, Scanning optical microscopy for porosity quantification of additively manufactured components, Addit. Manuf. (2018), https://doi.org/10.1016/j.addma.2018.03.019.
[70] M.S. Xavier, S. Yang, C. Comte, A. Bab-Hadiashar, N. Wilson, I. Cole, Nondestructive quantitative characterisation of material phases in metal additive manufacturing using multi-energy synchrotron X-rays microtomography, Int. J. Adv. Manuf. Technol. 106 (2020) 1601–1615, https://doi.org/10.1007/s00170-019-04597-y.
[71] M.R. Khosravani, T. Reinicke, On the use of X-ray computed tomography in assessment of 3D-printed components, J. Nondestruct. Eval. 39 (2020) 75, https://doi.org/10.1007/s10921-020-00721-1.
[72] J. Guan, X. Zhang, Y. Jiang, Y. Yan, Insights into fabrication mechanism of pure copper thin wall components by selective infrared laser melting, Rapid Prototyp. J. (2019), https://doi.org/10.1108/RPJ-06-2018-0143.
[73] A. Noskov, T.K. Ervik, I. Tsivilskiy, A. Gilmutdinov, Y. Thomassen, Characterization of ultrafine particles emitted during laser-based additive manufacturing of metal parts, Sci. Rep. 10 (2020) 20989, https://doi.org/10.1038/s41598-020-78073-z.
[74] M. Kunieda, A. Suzuki, N. Takata, M. Kato, M. Kobashi, Introducing hatch spacing into deposited energy density toward efficient optimization of laser powder bed fusion process parameters, Mater. Trans. 64 (2023) 1099–1106, https://doi.org/10.2320/matertrans.MT-ME2022002.
[75] X. Yan, C. Chang, D. Dong, S. Gao, W. Ma, M. Liu, H. Liao, S. Yin, Microstructure and mechanical properties of pure copper manufactured by selective laser melting, Mater. Sci. Eng. A (2020), https://doi.org/10.1016/j.msea.2020.139615.
[76] J.J. Marattukalam, D. Karlsson, V. Pacheco, P. Beran, U. Wiklund, U. Jansson, B. Hjörvarsson, M. Sahlberg, The effect of laser scanning strategies on texture, mechanical properties, and site-specific grain orientation in selective laser melted 316L SS, Mater. Des. (2020), https://doi.org/10.1016/j.matdes.2020.108852.